Bagnold Dunes campaign Phase 2: Visible/near-infrared reflectance spectroscopy of longitudinal ripple sands

Jeffrey R. Johnson[1], James F. Bell III[2], Steve Bender[3], Edward Cloutis[4], Bethany Ehlmann[5,6], Abigail Fraeman[5], Olivier Gasnault[7],Sylvestre Maurice[7], Patrick Pinet[7], Lucy Thompson[8], Danika Wellington[2], Roger C. Wiens[9]

[1]Johns Hopkins University Applied Physics Laboratory, 11101 Johns Hopkins Road 200-W230 Laurel, MD 20723-6005

[2]Arizona State University School of Earth and Space Exploration PO Box 871404 Tempe, AZ 85287-1404

[3]Planetary Science Institute, 1700 East Fort Lowell, Suite 106 Tucson, AZ 85719-2395

[4]University of Winnipeg, 515 Portage Avenue Winnipeg, Manitoba CANADA R3B 2E9

[5]Jet Propulsion Laboratory, 4800 Oak Grove Dr, Pasadena, CA 91109

[6]California Institute of Technology, 1200 E California Blvd, Pasadena, CA 91125

[7]Université de Toulouse, CNRS, Institut de Recherche en Astrophysique et Planetologie, 9 Avenue du Colonel Roche, 31400 Toulouse, France

[8]University of New Brunswick, 3 Bailey Dr, Fredericton, NB E3B 5A3, Canada

[9]Los Alamos National Laboratory, P.O. Box 1663 Los Alamos, NM 87545

Corresponding author: Jeffrey R. Johnson (jeffrey.r.johnson@jhuapl.edu)

Key Points:

- Bagnold Phase 2 sands exhibit higher 535 nm band depths and red/blue ratios, and lower 600/700 nm ratios than Bagnold Phase 1 sands
- Phase 2 sands contain a greater amount of redder, ferric materials, likely owing to minor hematite contamination from nearby bedrock

This article has been accepted for publication and undergone full peer review but has not been through the copyediting, typesetting, pagination and proofreading process which may lead to differences between this version and the Version of Record. Please cite this article as doi: 10.1029/2018GL079025

Abstract

As part of the Phase 2 Bagnold Dune campaign at Gale Crater, Mars, constraints on the geochemistry, mineralogy, and oxidation state of pristine and disturbed linear sand ripples were made using visible/near-infrared spectral observations for comparison to Phase 1 spectra of the barchan dunes to the north. Spectra acquired by the ChemCam and Mastcam instruments (400-1000 nm) at four Phase 2 locations revealed similar overall spectral trends between the two regions, but most Phase 2 sands were redder in the visible wavelengths. The majority of targets exhibited lower red/infrared ratios, higher ~530 nm band depths, and higher red/blue ratios than Phase 1 samples, suggesting a greater proportion of redder, fine-grained, ferric sands in Phase 2 samples. This is consistent with the slightly greater proportion of hematite in Phase 2 samples as determined from CheMin analyses of the Ogunquit sands, which may reflect contamination from the surrounding hematite-bearing Murray formation bedrock.

1 Introduction

Understanding the provenance and evolution of windblown sands on Mars requires a combination of regional and local analyses of their geochemical and mineralogical diversity. During Phase 1 of the Bagnold Dune campaign conducted by the Mars Science Laboratory Curiosity (Sols 1181-1254) the barchan dunes in the Namib and High Dune areas were investigated (Bridges and Ehlmann, 2018; Ehlmann et al., 2017). Phase 2 of the campaign (Sols 1601-1653) studied ripple fields and linear dunes in the Mount Desert Island and Nathan Bridges Dune regions 2 km to the south and ~100 m higher in elevation (Lapôtre and Rampe, 2018). Both campaigns acquired visible/near-infrared (400-1000 nm) reflectance spectra of pristine, disturbed, and sieved sands using Mast Camera (Mastcam) multispectral imaging (445–1013 nm) and Chemistry and Camera (ChemCam) passive point spectroscopy (400–840 nm). Johnson et al. (2017) reported that the Phase 1 dune sands were distinct from other martian dusty sands and typically exhibited low relative reflectance, weak ~530 nm absorption bands, an absorption band near 620 nm, and a decrease in spectral reflectance longward of ~685 nm. These characteristics were consistent with dominantly olivine-bearing sands, with likely contributions from high-calcium pyroxene (cf. Lapôtre et al., 2017). However, variations were observed between the finer and coarser-grained sands. Fine sands exhibited higher 535 nm absorption band depths and lower 600/700 nm spectral ratios, consistent with a combination of ferric materials (e.g., hematite, magnetite, nanophase and/or

amorphous oxides). Conversely, the coarsest grains (in ridge crests, lee slopes) were the darkest and bluest, with strong reflectance downturns in the near-infrared, higher 600/700 nm ratios (flatter spectra in this region) and near-zero 535 nm band depths, consistent with greater proportions of mafic silicate minerals.

We report here analyses of Mastcam and ChemCam reflectance data acquired during the Phase 2 campaign, which comprised four stops along the rover traverse (Figure 1). The first three of these stops (Mapleton, Sandy Point Beach, and Southern Cove) sampled locations on the eastern margin of Nathan Bridges Dune (Figures S1-S4). The fourth stop was on the western edge of Mount Desert Island at Ogunquit Beach (Figure S5), where scooped sands were sieved for onboard analyses (Rampe et al., 2018; Stern et al., 2018). The pre-sieved (>150 μm) and post-sieved (<150 μm) samples were kept onboard the rover until they were dumped on Sol 1968 and analyzed with Mastcam and ChemCam shortly thereafter (Figure S6).

2 Methodology

2.1 ChemCam passive spectra

The ChemCam instrument is used for laser-induced breakdown spectroscopy (LIBS) in which light from a laser-generated plasma is dispersed onto three spectrometers to detect elemental emission lines at high spectral resolution (< 1 nm) (Wiens et al. 2013, 2015). Relative reflectance spectra (400-840 nm) can be collected in passive mode (i.e., without using the laser) for each sunlit location to provide information on variations in ferrous and ferric components (Johnson et al., 2015, 2016, 2017). For materials near the rover (~2-7 m) the 0.65 mrad field of view of each point measurement sampled areas 1.3-4.5 mm. Each LIBS measurement included a 3 msec exposure passive ("dark") measurement used to subtract ambient light from the LIBS spectrum. Because the laser shock wave creates pits in the sands, passive measurements shown here were acquired prior to its use to avoid pit shadows. Passive measurements at 30 msec exposures were acquired for specific targets to increase the signal to noise ratio (SNR). Data acquired on Sol 76 at 12:52 Local True Solar Time (LTST) of the white ChemCam calibration target holder were used to minimize dark current variations between scene and calibration targets. Raw data were converted to radiance (Johnson et al., 2015), with an estimated absolute 6-8% calibration uncertainty. The ratio of the scene and Sol 76 calibration target radiance was multiplied by the laboratory reflectance

of the calibration target material (Wiens et al. 2012) to provide relative reflectance. Images from the Remote Micro-Imager (RMI) were acquired to provide accurate positions for raster locations (Wiens et al. 2012, 2015; Maurice et al. 2012, 2016; Le Mouélic et al. 2015) (Figure S6).

We calculated spectral parameters using ±5 nm averages around a central wavelength. Near-infrared ratios (e.g., 600/700 nm) and peak reflectance wavelengths are indicative of the strength of iron absorptions from mafic minerals, and 600/440 nm (red/blue) ratios are sensitive to oxidation state and/or dust deposition. The 535 nm band depth (calculated using shoulders at 500 nm and 600 nm) is sensitive to the presence of crystalline ferric oxides (e.g., Morris et al. 1997, 2000; Bell et al. 2000).

2.1 Mastcam passive spectra

The Mastcam system includes two cameras (M100, 100 mm focal length; M34, 34 mm focal length) that use 1600x1200 pixel Bayer-patterned CCDs. Each uses 6 narrow band (±10 nm) filters to characterize the 445-1013 nm reflectance spectra of surface targets. One filter position has a broadband infrared-cutoff filter for RGB color imaging using a Bayer pattern bonded directly to the detectors (Wellington et al., 2016). The two cameras provide twelve center wavelengths for multispectral analysis, including the three RGB Bayer bands (which have ± 40 nm bandwidths). Wellington et al. (2017) and Bell et al. (2003, 2017) describe conversion of raw Mastcam data to radiance ($W/m^2/nm/sr$) and to radiance factor (I/F) using observations of the onboard Mastcam calibration target (Kinch et al., 2015; Wellington et al., 2016; He et al. 1991; Bell et al. 2003). Radiance factors were divided by the cosine of the solar incidence angle to provide relative reflectance (R*), an approximation of the reflectance factor defined in Hapke (1993, 2012). Relative reflectance spectra presented here are average values derived from manually defined regions selected of the same region in the M34 and M100 images. M100 filter values were scaled to the left eye at the 1013 nm wavelength (which is least affected by uncertainties in the dust correction) and averaged with the M34 values at overlapping wavelengths to produce a combined spectrum. The absolute radiometric accuracy for Mastcam is estimated to be 10-20%, with a filter-to-filter uncertainty of <5% and pixel-to-pixel variation of <1% (Bell et al. 2003, 2017; Wellington et al. 2016).

Mastcam spectral parameters were calculated using wavelengths similar to the ChemCam spectral parameters. Parameters sensitive to ferric crystallinity, oxidation state

and/or dust deposition included the band depth at 527 nm (calculated using shoulders at 494 nm and 639 nm), the peak reflectance position, and the 639/446 nm ratio. Near-infrared parameters (676/751 nm ratio) are sensitive to mafic silicate minerals.

3 Data sets used

Table 1 lists the ChemCam and Mastcam data sets acquired at each Stop that were used in this analysis. At Stop 1, Mastcam observations were acquired of undisturbed and Alpha Particle X-Ray Spectrometer (APXS)-disturbed ripple sands at Matagamon, and two locations on pristine and rover wheel-disturbed sands in the Scarboro area (Figures S1-S2). ChemCam data were acquired at Mapleton. At Stop 2, Mastcam imaging at Macworth documented rover tracks and pristine sands (Figure S3), while ChemCam observations sampled the edge of a rover track (Macworth) and ripple crests (Towow, Leighton, Carrassett, Swanback). Between Stops 2 and 3 ChemCam observed the ripple crest Mattawamkeag. At Stop 3, Mastcam targeted the pristine and disturbed sands at Hildreths (Figure S4), while ChemCam observed disturbed sands at Greenvale Cove and the ripple crests Ripogenus (Figure S7) and Spragueville (acquired twice owing to shadows obscuring raster locations 7-10 during the first attempt). At Stop 4, Mastcam observed pristine and rover-disturbed sands near Ogunquit (Figure S5), and ChemCam acquired spectra on a rover scuff wall (Tumbledown Mountain), the base of that wall (Elephant Mountain) and on the scuff floor (Canoe Point). Undisturbed sand was observed at North Brother, and ripple crests of different sizes were sampled at Hamlin Peak (small), Avery Peak (medium), and Baxter Peak (large; Figure S7). Unused portions of the Ogunquit sand samples were kept onboard until Sol 1970, when the post-sieve (< 150 μm) and pre- sieve (>150 μm) samples were dumped onto bedrock while the rover was on Vera Rubin Ridge (VRR) and analyzed by Mastcam and using dedicated passive and active ChemCam methods (Figures S6, S8-S10).

4 Results

4.1 ChemCam and Mastcam spectra

Representative Chemcam passive and Mastcam relative reflectance spectra from the four stops are shown in Figure 2. Spectral differences among disturbed, undisturbed, and ripple crest/trough sands are marked by changes in the visible spectral slope, maximum reflectance position, and the steepness of the near-infrared slope. These are due to variations in the relative abundance and/or grain size of mafic minerals (olivines, pyroxenes) versus finer-grained, more ferric, oxidized materials, particularly in the disturbed sands, modulated by the

effects of amorphous components (e.g., Achilles et al., 2017; Rampe et al., 2018). In the Mapleton and Towow areas, ChemCam spectra are typical of reddish sands observed elsewhere throughout the traverse (Johnson et al., 2015, 2016). The crest of the Ripogenus ripple exhibited reflectance maxima at shorter wavelengths than the flank, consistent with more ferrous materials on the crest (cf. Figure S7). The spectral shapes of nearby Sprague ville sands were nearly identical to the Ripogenus flank. The Baxter Peak ripple target's crest showed the strongest near-infrared downturn, consistent with more ferrous sands compared to the trough (cf. Figure S7). In enhanced Mastcam color images, the coarser disturbed sands in the Hildreths area appear bluish (Figure S4). The corresponding Mastcam spectra in Figure 2b show a maximum reflectance near 675 nm compared to a maximum reflectance position near 750 nm associated with redder sands of Macworth and Ogunquit. Similar shorter-wavelength maxima were observed for bluer regions at the Ogunquit area and the ripple crest target Scarboro in the Mapleton area. For comparison, redder sands in the troughs of scuff areas and flanks of ripples in the Scarboro area exhibited longer-wavelength maxima. In summary, ripple crests (e.g., Ripogenus, Baxter Peak, Scarboro) and collections of coarser grains in disturbed soils (e.g., Hildreths, Ogunquit) tend to exhibit reflectance peaks at shorter wavelengths, steeper near-infrared downturns, and weak to nonexistent ~530 nm band depths, consistent with more ferrous materials compared to the redder, more ferric ripple flanks or troughs.

The Ogunquit pre- and post-sieve dumped samples exhibited very similar ChemCam passive and Mastcam relative reflectance spectra (Figures 3, S6), with ~530 nm and 867 nm absorption bands in both samples. Nearby background sand exhibited similar Mastcam spectra, albeit with some variations in the strength of the 867 nm band. This is evident in the Mastcam 867 nm band depth image (Figure S8) in which the dumped samples and background sands are essentially indistinguishable. However, the 527 nm band depth images showed that the dumped samples were slightly brighter than the background sands (Figures S8-S10), and the decorrelation stretch images manifest this with more purple hues in the dump piles. This spectral behavior suggests a greater proportion of ferric oxides in the Ogunquit sieved sands. Rampe et al. (2018) discuss the possible contamination of this sample by remnants of the previously drilled, hematite-rich sample Sebina. However, they

did not estimate hematite contamination and concluded from Chemistry and Mineralogy (CheMin) data that minor (1.2 wt%) hematite is likely present in the crystalline+amorphous portion of the Ogunquit < 150 μm sample.

4.2 Spectral parameters

Spectral parameters computed from ChemCam spectra are shown in Figure 4, where the 600/700 nm (red/infrared) ratio is compared to the 535 nm band depth and 600/440 nm (red/blue) ratio. Parameters from representative Phase 1 targets are shown for comparison (square symbols). Phase 2 samples were redder (higher 600/440 nm ratios) than most Phase 1 samples, with lower red/near-infrared ratios. Exceptions were the bluer portions of ripple crests with higher red/infrared ratios (e.g., Baxter Peak, Ripogenus), which transitioned into redder, more ferric materials along the flanks or troughs of the ripples, as shown schematically by the orange arrows in Figure 4. The Ogunquit dump samples exhibited high 535 nm band depths but were among the least red Phase 2 samples, similar to the Dump E (< 150 μm) sands from Phase 1.

Figure 5 shows similar spectral parameters computed from Mastcam spectra from both campaign Phases, where the 676/751 nm (red/infrared) ratio is compared to the 527 nm band depth and the 639/446 (red/blue) ratio. Nearly all Phase 2 samples were redder with stronger 527 nm band depths than Phase 1 sands, with low red/infrared ratios closer to the < 150 μm Phase 1 sieved samples. The exceptions were the bluer, coarser disturbed sands from Hildreths, Ogunquit, and Matagamon, which exhibited the weakest 527 nm band depths and highest red/infrared ratios, transitioning to finer, redder sands as shown schematically by the arrows (cf. Figures S1-S5). The Ogunquit samples were much less red than other Phase 2 samples and most similar to Phase 1 sands. However, their 527 nm band depths and red/infrared ratios were similar to the other Phase 2 sands.

5 Discussion and Conclusions

Based on their higher ~530 nm band depths and red/blue ratios and lower red/infrared ratios, we interpret that most of the Phase 2 sands contained greater proportions of redder, fine-grained, ferric materials than Phase 1 sands. However, several of the bluer, coarser-grained Phase 2 ripple crests were similar to Phase 1 sands, and some exhibited higher red/infrared ratios for a given red/blue ratio than Phase 1 sands (e.g., Hildreths, Baxter Peaks' crest in

Figure 5b). This likely resulted from the more active wind regime in this region (cf. Baker et al., 2018; Lapôtre et al., 2018), which limited dust contamination and exposed more ferrous sands. Indeed, APXS analyses suggested low dust content (implied from low S, Cl and Zn concentrations), particularly for the more mafic ripple crests which contained relatively greater amounts of Mg and Ni, compared to enrichments in Ti and Cr in off-crest sands (O'Connell-Cooper et al., 2018). By comparison, the sieved Ogunquit samples exhibited strong ~530 nm band depths but an overall less red appearance than other Phase 2 sands even though APXS analyses suggested higher dust contributions. We conclude that Phase 2 sands contained minor, detrital, hematite-rich particles sourced from the surrounding bedrock of the Murray formation in addition to relatively lower proportions of mafic minerals. Analyses by Rampe et al. (2018) suggested lower olivine and higher plagioclase abundances in the crystalline portion of the < 150 μm Ogunquit fraction than in the Phase 1 Gobabeb samples, along with ~2 wt% hematite. The proportion of crystalline hematite was likely larger in the Phase 2 sands, and/or the grain size distribution of hematite was smaller, in order to account for their stronger ~530 nm bands. In addition, images from the Mars Hand Lens Imager (MAHLI) suggested the presence of reddish outcrop fragments < 500 mm in size, although the average grain size was smaller in the Phase 2 dune sands than Phase 1 (Weitz et al., 2018). Analyses of sands along the rest of the Curiosity rover traverse will continue to document compositional and mineralogical variations and potential bedrock contributions from the stratigraphy of Mt. Sharp.

Acknowledgments, Samples, and Data

This work was funded by the NASA Mars Science Laboratory Participating Scientist program through the Jet Propulsion Laboratory (contracts 1350588 and 1546033). A portion of this research was carried out at JPL, under a contract with NASA. The US portion of ChemCam and MSL rover operations was funded by NASA's Mars Exploration Program. The French contribution to MSL is supported by CNES. The authors thank the operations teams involved in acquiring these data sets. Original data that underlie the conclusions presented in this manuscript can be found on the NASA Planetary Data System and/or in the relevant references cited. The authors fondly recall the dedicated efforts toward the Bagnold Dune campaigns by our late colleague Dr. Nathan Bridges.

References

Achilles, C. N., et al. (2017), Mineralogy of an active eolian sediment from the Namib dune, Gale crater, Mars, J. Geophys. Res. Planets, 122, 2344–2361, doi: 10.1002/2017JE005262.

Bell, J. F., H. Y. McSween, J. A. Crisp, R. V. Morris, S. L. Murchie, N. T. Bridges, J. R. Johnson et al, Mineralogic and compositional properties of Martian soil and dust: Results from Mars Pathfinder, *Journal of Geophysical Research: Planets* 105, no. E1: 1721-1755, 2000.

Bell, J.F., III, Squyres, S.W., Herkenhoff, K.E., Maki, J.N., Arneson, H.M., Brown, D., Collins, S.A., Dingizian, A., Elliot, S.T., Hagerott, E.C., and others, Mars Exploration Rover Athena Panoramic Camera (Pancam) investigation. *Journal of Geophysical Research: Planets*, 108, 8063, 2003.

Bell, J. F., III et al. (2017), The Mars Science Laboratory Curiosity rover Mastcam instruments: Preflight and in-flight calibration, validation, and data archiving, Earth and Space Science, 4, doi:10.1002/2016EA000219.

Bridges, N. T., and Ehlmann, B. L. (2018). The Mars Science Laboratory (MSL) Bagnold Dunes campaign, Phase I: Overview and introduction to the special issue. *Journal of Geophysical Research: Planets*, 123(1), 3-19.

Ehlmann, B. L., Ehlmann, B.L., Edgett, K.S., Sutter, B., Achilles, C.N., Litvak, M.L., Lapotre, M.G., Sullivan, R., Fraeman, A.A., Arvidson, R.E., Blake, D.F. and Bridges, N.T., (2017), Chemistry, mineralogy, and grain properties at Namib and High dunes, Bagnold dune field, Gale crater, Mars: A synthesis of Curiosity rover observations, *J. Geophys. Res*. Planets, 122, doi:10.1002/ 2017JE005267.

Hapke, B., Theory of Reflectance and Emittance Spectroscopy, Cambridge University Press, 455 pp., 1993.

Hapke, B., Theory of Reflectance and Emittance Spectroscopy, 2nd edition, Cambridge Univ. Press, 520 pp., 2012.

He, X.D., Torrance, K.E., Sillion, F.X., and Greenberg, D.P., A comprehensive physical model for light reflection. Proceedings of the 18th Annual Conference on Computer Graphics and Interactive Techniques, 175–186, 1991.

Johnson, J.R., J.F. Bell III , S. Bender , D. Blaney , E. Cloutis , L. DeFlores , B. Ehlmann, O. Gasnault , B. Gondet , K. Kinch , M. Lemmon, S. Le Mouélic , S. Maurice , M. Rice, R. Wiens, MSL Science Team, ChemCam Passive Reflectance Spectroscopy of Surface Materials at the Curiosity Landing Site, Mars, *Icarus*, 249, 74–92, http://dx.doi.org/10.1016/j.*Icarus*.2014.02.028, 2015.

Johnson, J.R., J. F. Bell III, S. Bender, D. Blaney, E. Cloutis, B. Ehlmann, A. Fraeman, O. Gasnault, K. Kinch, S. Le Mouélic, S. Maurice, E. Rampe, D. Vaniman, R.C. Wiens, Constraints on iron sulfate and iron oxide mineralogy from ChemCam visible/near-infrared reflectance spectroscopy of Mt. Sharp basal units, Gale Crater, Mars, Amer. Mineralogist, 101, 1501–1514, 2016.

Johnson, J.R., C. Achilles, J. F. Bell III, S. Bender, E. Cloutis, B. Ehlmann, A. Fraeman, O. Gasnault, V.E. Hamilton, S. Le Mouélic, S. Maurice, P. Pinet, L. Thompson, D. Wellington, R.C. Wiens, Visible/near-infrared spectral diversity from in situ observations of the Bagnold Dune Field sands in Gale Crater, Mars, J. Geophys. Res., 122, doi:10.1002/2016JE005187, 2017.

Kinch, K. M., J. F. Bell III, W. Goetz, J. R. Johnson, J. Joseph, M. B. Madsen, and J. Sohl-Dickstein, Dust deposition on the decks of the Mars Exploration Rovers: 10 years of dust dynamics on the Panoramic Camera calibration targets, Earth and Space Science, 2, doi:10.1002/2014EA000073, 2015.

Lapôtre, M.G., and E. Rampe, (2018), Curiosity's investigation of the Bagnold Dunes, Gale crater: Overview of the two-phase campaign and introduction to the special collection, *Geophys. Res. Lett.,* this issue.

Lapôtre, M. G. A., B. L. Ehlmann, S. E. Minson, R. E. Arvidson, F. Ayoub, A. A. Fraeman, R. C. Ewing, and N. T. Bridges (2017), Compositional variations in sands of the Bagnold Dunes, Gale crater, Mars, from visible-shortwave infrared spectroscopy and comparison with ground truth from the Curiosity rover, *J. Geophys. Res*. Planets, 122, doi:10.1002/2016JE005133.

Lapôtre, Ewing, Weitz, Lewis, Rubin, Lamb, Ehlmann, Bridges, (2018), Morphologic diversity of martian ripples: Implications for low-intensity transport as a mechanism for large-ripple formation, *Geophys. Res. Lett.*, this issue.

Le Mouélic S., Gasnault O., Herkenhoff K.E., Bridges N.T., Langevin Y., Mangold N., Maurice S., Wiens R.C., Pinet P., Newsom H.E., Deen R.G., Bell III J.F., Johnson J.R., Rapin, W., Barraclough B., Blaney D.L., Deflores L., Maki J., Malin M.C., Pérez R., and Saccoccio M., The ChemCam Remote Micro-Imager at Gale crater : review of the first year of operations on Mars, *Icarus*, 249, 93-107, 2015.

Maurice, S., et al., The ChemCam instrument suite on the Mars Science Laboratory (MSL) rover: Science objectives and mast unit description, *Space Sci. Rev*., 170, 95–166, doi:10.1007/s11214-012-9912-2, 2012.

Maurice, S., et al., ChemCam Activities and Discoveries during the Nominal Mission of Mars Science Laboratory in Gale crater, Mars, *Journal of Analytical Atomic Spectrometry*, published by the Royal Society of Chemistry, DOI: 10.1039/c5ja00417a, 2016.

Morris, R.V., D.C. Golden, J.F. Bell III, Low-temperature reflectivity spectra of red hematite and the color of Mars, Journal of Geophysical Research, 102, 912-9133, 1997.

Morris, R. V., et al., Mineralogy, composition, and alteration of Mars Pathfinder rocks and soils: Evidence from multispectral, elemental, and magnetic data on terrestrial analogue, SNC meteorite, and Pathfinder samples, *J. Geophys. Res*., 105, 1757–1817, doi:10.1029/1999JE001059, 2000.

Rampe, E.B., T. F. Bristow, D. F. Blake, D. T. Vaniman, C. N. Achilles, R. E. Arvidson, N. Castle, S. J. Chipera, P. I. Craig, D. J. Des Marais, R. T. Downs, J. Farmer, R. Hazen, B. Horgan, M. Lapotre, D. W. Ming, R. V. Morris, S. M. Morrison, T. S. Peretyazhko, A. H.

Treiman, V. Tu, and A. S. Yen, 2018, Mineralogy of the Bagnold Dunes sands, Gale crater, as derived in situ and from orbit, this issue.

Stern, J., B. Sutter, D. Archer, A. McAdam, C. Malespin, and P. Mahaffy, 2018, Volatile inventory of eolian materials in Gale Crater, this issue.

Wellington, D.F., Bell, J.F., Johnson, J.R., Kinch, K.M., Rice, M.S., Godber, A., Ehlmann, B.L., Fraeman, A.A. and Hardgrove, C., 2017. Visible to near-infrared MSL/Mastcam multispectral imaging: Initial results from select high-interest science targets within Gale Crater, Mars. American Mineralogist, 102(6), pp.1202-1217.

Weitz, C.M., R.J. Sullivan, M. G. A. Lapotre, S. K. Rowland, J. A. Grant, M. Baker, and R. Aileen Yingst, Sand grain sizes and shapes in eolian bedforms at Gale Crater, Mars, Geophys. Res. Lett., this issue, 2018.

Wiens, R. and 80 others, The ChemCam Instrument Suite on the Mars Science Laboratory (MSL) Rover: Body Unit and Combined System Performance, Space Sci Rev., 170, 167-227, 2012.

Wiens, R. C., et al., Pre-flight calibration and initial data processing for the ChemCam laser-induced breakdown spectroscopy instrument on the Mars Science Laboratory rover, Spectrochimica Acta Part B: Atomic Spectroscopy 82, 1-27, 2013.

Wiens, R.C., S. Maurice, and the MSL Science Team ChemCam: Chemostratigraphy by the first Mars microprobe, Elements, 11(1):33-38, doi:10.2113/gselements.11.1.33, 2015.

Table 1. ChemCam and Mastcam sequences used.

Target	Stop #	Sol	Sequence ID	LTST (start)	Raster Size column x row
Mapleton	1	1602	ccam1602	12:11	5x1
New Sweden	2	1617	ccam1617	10:26	1x5
Macworth	2	1618	ccam3618	10:44	1x10
Towow	2	1618	ccam1618	10:18	5x1
Leighton	3	1623	ccam2623	12:30	10x1
Carrassett	3	1625	ccam1625	11:43	10x1
Swanback	3	1627	ccam1627	11:42	1x10
Mattawamkeag	2/3	1630	ccam2630	12:45	1x5
Ripogenus	3	1637	ccam2637	10:35	1x10
Sprague ville	3	1637	ccam1637	10:06	1x10
Sprague ville_2	3	1638	ccam02638	12:12	1x10
Greenvale Cove	3	1639	ccam1639	11:49	1x7
Tumbledown Mountain	4	1652	ccam1652	11:18	5x1
Elephant Mountain	4	1652	ccam2652	11:32	5x
Canoe Point	4	1652	ccam3652	11:48	5x1
North Brother	4	1653	ccam1653	11:04	5x1
Avery Peak	4	1653	ccam2653	11:19	10x1
Baxter Peak	4	1653	ccam3653	14:15	10x1
Ogunquit postsieve passive	--	1970	ccam5968	12:27	5x1
Ogunquit presieve passive	--	1971	ccam1971	13:24	5x1
Ogunquit postsieve active	--	1971	ccam2971	13:33	5x1
Ogunquit presieve active	--	1972	ccam1972	12:53	5x1
Matagamon	1	1603	mcam08177	12:40	---
Scarboro	1	1603	mcam08179	12:50	---
Macworth	2	1618	mcam08273	11:28	---
Hildreths	3	1637	mcam08465	11:12	---
Ogunquit	4	1652	mcam08558	10:50	---
Ogunquit dump	--	1970	mcam10306	12:07	---

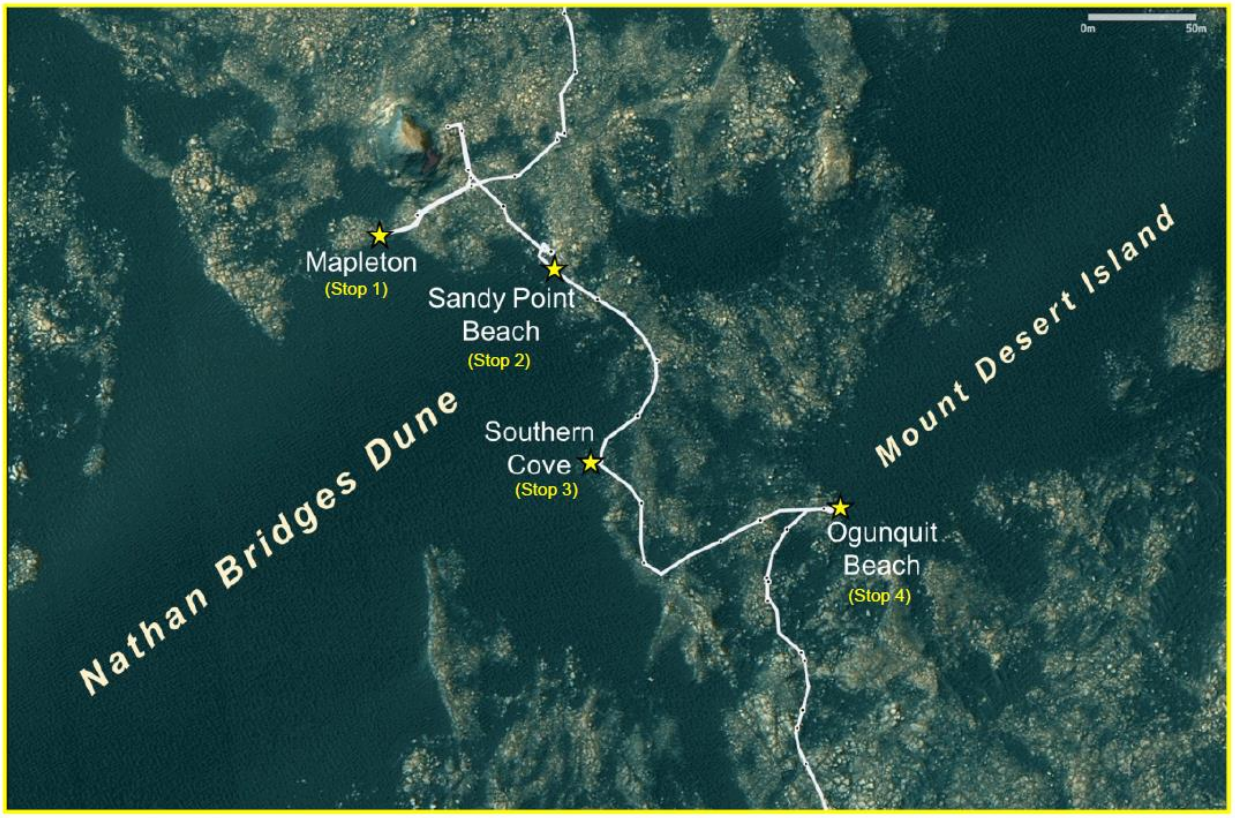

Figure 1. HiRISE orbital color scene of Phase 2 region, showing rover traverse (white) and four stops made during the campaign. Background image is HiRISE ESP_035772_1755.

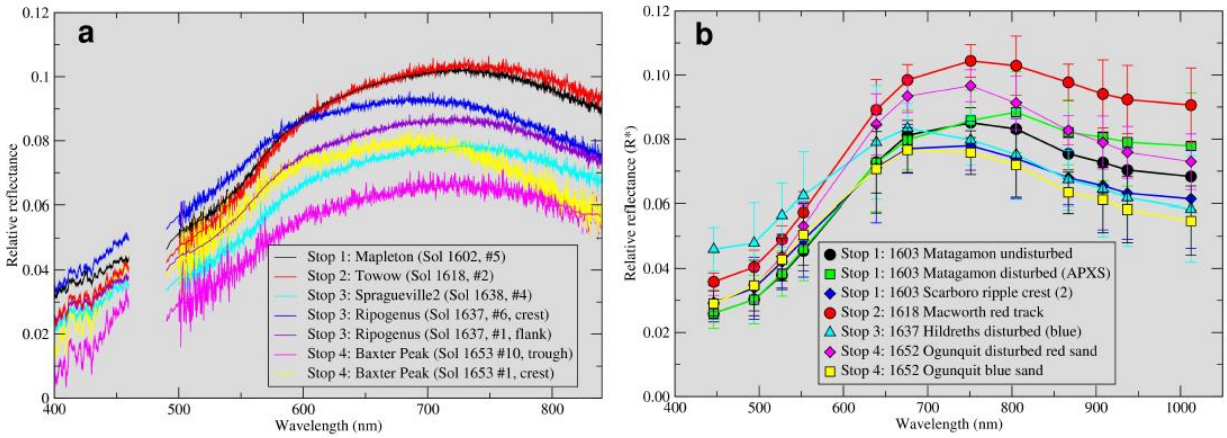

Figure 2. (a) ChemCam passive reflectance spectra of representative samples acquired at the four stops of the Phase 2 campaign. Legend shows Sol number and raster location number in parentheses. Gap between 468-478 nm represents region between ChemCam detectors. Each spectrum includes a 50-channel average line overlain; only this average is shown in the 400-500 nm region owing to low SNR in this region. (b) Mastcam relative reflectance spectra of representative samples acquired at the four stops. Error bars represent standard deviation of region of interest selected (see Figures S1-S5 for locations from which spectra were extracted).

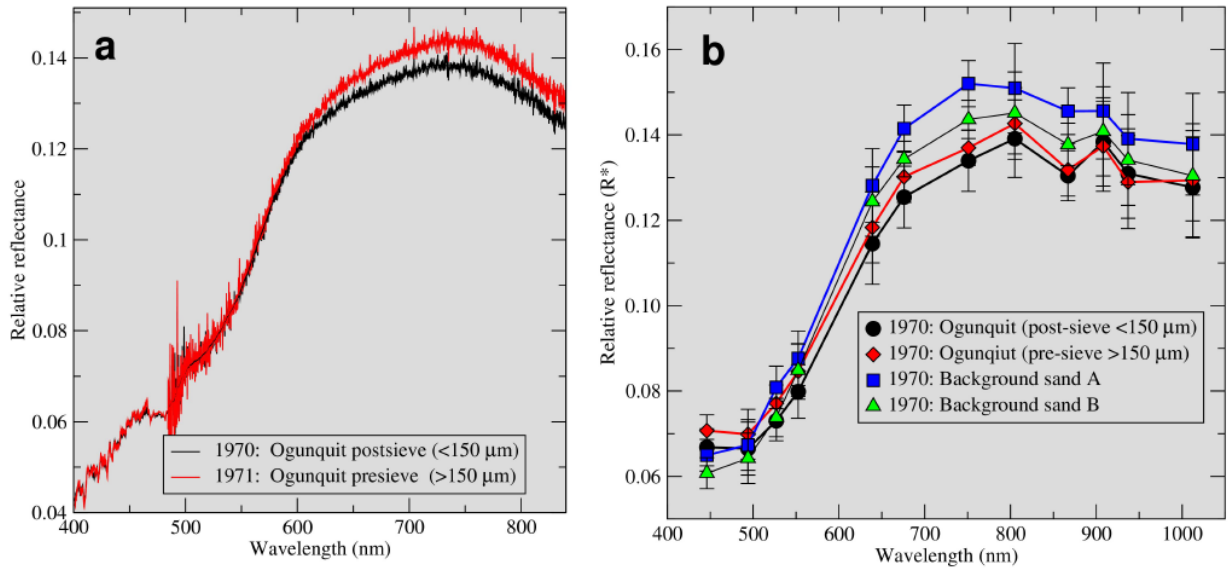

Figure 3. (a) ChemCam passive reflectance spectra of Ogunquit pre-sieved (150 >µm) and post-sieved (<150 µm) dumped samples. (b) Mastcam relative reflectance spectra of Ogunquit dumped samples (extracted from same area sampled by ChemCam raster, cf. Figure S6) compared to spectra of background sands in the same scene.

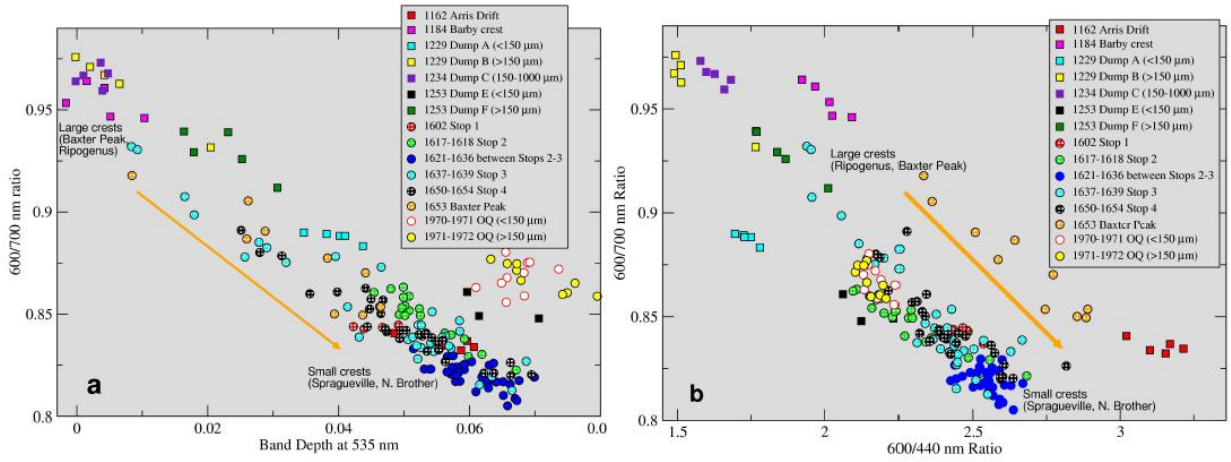

Figure 4. ChemCam spectral parameters for Phase 2 (circles) and representative Phase 1 samples (squares) (cf. Johnson et al., 2017). (a) 535 nm band depth versus 600/700 nm ratio; (b) 600/440 nm ratio vs. 600/700 nm ratio. Orange arrow points from coarser, more ferrous sands on larger ripple crests to finer, more ferric sands on smaller ripple crests.

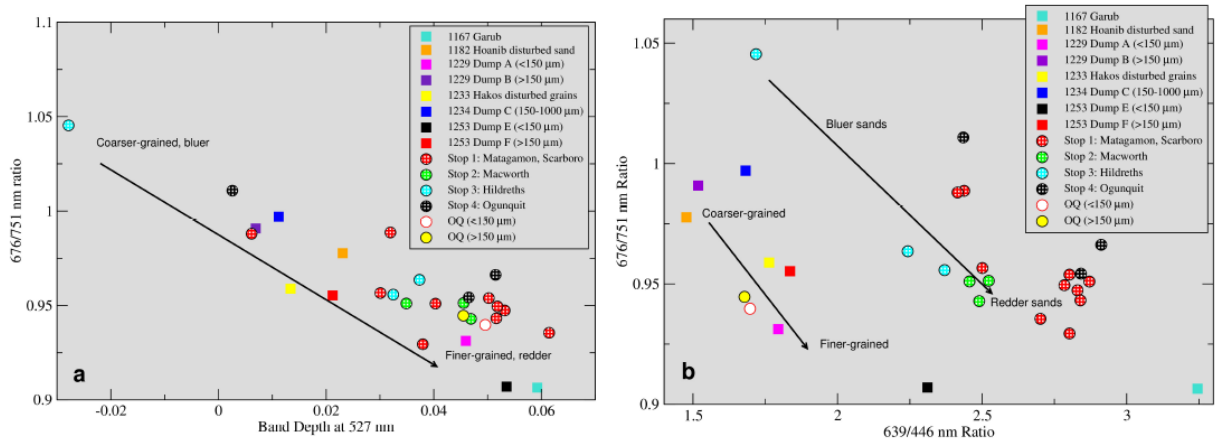

Figure 5. Mastcam spectral parameters for Phase 2 (circles) and representative Phase 1 samples (squares) (cf. Johnson et al., 2017). (a) 527 nm band depth versus 676/751 nm ratio; (b) 639/446 nm ratio vs. 676/751 nm ratio. Black arrows point from coarser, bluer, more ferrous sands on larger ripple crests to finer, more red, ferric sands on smaller ripple crests.